Flyby Characterization of Lower-degree Spherical Harmonics around Small Bodies

Yu Takahashi* Stephen Broschart*and Gregory Lantoine*

Jet Propulsion Laboratory, 4800 Oak Grove Drive, Pasadena, California, 91109

Interest in studying small bodies has grown significantly in the last two decades, and there are a number of past, present, and future missions. These small body missions challenge navigators with significantly different kinds of problems than the planets and moons do. The small bodies' shape is often irregular and their gravitational field significantly weak, which make the designing of a stable orbit a complex dynamical problem. In the initial phase of spacecraft rendezvous with a small body, the determination of the gravitational parameter and lower-degree spherical harmonics are of crucial importance for safe navigation purposes. This motivates studying how well one can determine the total mass and lower-degree spherical harmonics in a relatively short time in the initial phase of the spacecraft rendezvous via flybys. A quick turnaround for the gravity data is of high value since it will facilitate the subsequent mission design of the main scientific observation campaign. We will present how one can approach the problem to determine a desirable flyby geometry for a general small body. We will work in the non-dimensional formulation since it will generalize our results across different size/mass bodies and the rotation rate for a specific combination of gravitational coefficients.

Nomenclature

G	Gravitational constant
M^*	Reference mass
GM	Gravitational parameter (i.e., GM^*)
R^*	Reference mass
P	Associated Legendre function
C, S	Spherical harmonic coefficients
U, $\bar{U}$	Dimensional and non-dimensional gravitational potentials
t, τ	Dimensional and non-dimensional times
r, $\mathscr{r}$	Dimensional and non-dimensional positions
V, $\mathscr{V}$	Dimensional and non-dimensional velocities
$\vec{a}$	Acceleration
$\bar{b}^*$	Non-dimensional basis function
Z	Measurement
$\vec{X}$	State vector
$\tilde{H}$, H	Measurement partials at the observation time and epoch
Φ	State transition matrix
Λ	Information matrix
P	Covariance matrix
Γ	Doppler-only approximation of the information matrix
W	Weight matrix
σ	Uncertainty
ϱ	Asteroid - Earth vector
$[BA]$	Rotation matrix from the inertial (A) frame to the body frame (B) of the asteroid

*Navigation and Mission Design Engineers, Mission Design and Navigation Section, Jet Propulsion Laboratory, 4800 Oak Grove Drive, Pasadena, California, 91109

$[RA]$ Rotation matrix from the inertial (A) frame to the RTN (R) frame

Super/subscript

n	Degree
m	Order
p	Periapsis
Dop	Doppler
Opnav	Optical navigation
sat	Spacecraft
ast	Asteroid
earth	Earth
Ben	Bennu
Ito	Itokawa
RTN	Radial - transverse - normal
0	Epoch (i.e., $t = t_0$)
k	Time stamp

I. Introduction

Interest in studying small bodies has grown significantly in the last two decades, and there are a number of past, present, and future missions. These small body missions pose different types of challenges to navigators than conventional large bodies such as planets and moons. The small bodies' shape is often irregular and their gravitational field significantly weak. Thus, the perturbations from the non-spherical gravitational coefficients and solar radiation pressure (SRP) are more significant around small bodies and can result in unstable orbit that will result in an impact to or escape from the body in the matter of days.[1] Often times the SRP would drives the orbit eccentricity up and gravity perturbs the orbit significantly near the periapsis, resulting in a chaotic development of the spacecraft orbit. However, contrary to the challenges, the weak perturbing forces allow the spacecraft to fly more freely. Hovering and multiple flybys (e.g., ping-pong maneuvers) are the two demonstrative cases that are not easily attainable with large bodies.

In the initial phase of spacecraft rendezvous with a small body, the determination of the gravitational parameter and lower-degree spherical harmonics are of crucial importance. An accurate estimation of these parameters is important for safe navigation of a spacecraft in a strongly perturbed environment typical of small bodies. Added benefits can be gained by quick and robust estimation procedure because such a mission design can enable earlier commencement of the science/observation campaigns. The usual procedure is to perform some number of hyperbolic flybys prior to orbit insertion because such mission design does not require rigorous stability analysis of the trajectory (i.e., robust to gravitational uncertainties).[2–4] This motivates studying how well one can determine the total mass and lower-degree spherical harmonics in a relatively short time in the initial phase of the spacecraft rendezvous. We will focus on this initial characterization phase where the gravity field is largely unknown, and investigate the accuracy with which we can determine some crucial parameters of the gravity field via slow, hyperbolic flybys.

The past research mainly investigated the effectiveness of Doppler for the GM (i.e., gravitational parameter) estimation. A number of resources are available for this task, where their focus is on high-speed flybys of asteroids during the cruise period to the main planetary/small body target[5–10] or flybys of moons during the planetary tour.[11,12] Both Anderson[13] and Sybert et al.[14] analytically looked at the covariance of the gravitational parameter (GM) assuming a linear trajectory under the two-body dynamics. This assumption is easily validated since their combination of the target radius and target speed yields the trajectory with high ($\gg 1$) eccentricity. Similar analytical approach is explored to estimate the gravitational parameter by Pätzold et al.,[6–8] where the total Doppler shift is related to GM. This formulation yields a point solution for GM when the real tracking data is available. On the other hand, Takahashi and Scheeres[2] discussed a numerical approach to determining the feasibility of the estimation of the lower-degree gravitational coefficients for different bodies.

In addition, the perturbations to the spacecraft trajectory due to the second-degree harmonics have been analytically solved before. For example, Anderson and Giampieri[15] and Rappaport et al.[16] investigated the perturbations to the hyperbolic trajectory due to C_{20} and C_{22} by variation of parameters. However, their formulation is such that the spacecraft trajectory is related to its dynamics through non-singular orbital

elements and perturbations to the local coordinate frame, which is not very useful for covariance analysis. Ultimately, we wish to compute the Doppler from the spacecraft state (i.e., position and velocity).

In this paper, we will perform the covariance analysis of the gravitational coefficients from a single flyby of Doppler and optical navigation (OpNav), for which we resort to numerical analysis. To this end, a least-squares filter is developed and its performance is numerically evaluated to provide an eye chart of the covariance performance with respect to the flyby radius and flyby speed. With this tool we will identify optimal flyby geometries to estimate GM, C_{20}, and C_{22}. The rest of the paper is organized as follows: we will first introduce the equations of motion of the spacecraft, the measurement models, and present the performance of the Doppler/OpNav covariance. For the rest of the paper, we would only consider the gravitational forces and do not deal with the SRP or other perturbation forces.

II. Non-dimensional Dynamics

There are over 10,000 near-Earth asteroids discovered and catalogued, and their shape as well as their gravity fields vary substantially from one body to another. Thus, it is sensible to derive the equations of motion in the non-dimensional space to generalize the problem. In the dimensional system, the spherical harmonic gravity field is expressed as

$$U = \frac{GM^*}{R^*}\sum_{n=0}^{\infty}\sum_{m=0}^{n}\left(\frac{R^*}{r}\right)^{n+1}P_{nm}(\sin\phi)\begin{bmatrix}\cos(m\lambda)\\ \sin(m\lambda)\end{bmatrix}\cdot\begin{bmatrix}C_{nm}\\ S_{nm}\end{bmatrix} \tag{1}$$

where U is the potential, G is the gravitational constant, M^* is the reference mass (nominally the total mass of the body), R^* is the reference radius (arbitrary, but convenient if set to the circumscribing radius of the body[17]), r is the spacecraft position, P_{nm} is the associated Legendre function of degree n and order m, C_{nm} and S_{nm} are spherical harmonic coefficients, λ is longitude, and ϕ is latitude in the body-fixed frame. The degree zero and order zero term is commonly referred to as the point-mass or two-body gravity field. The acceleration of the spacecraft is given by the partial of the potential with respect to the spacecraft coordinates.

A. Two-body Dynamics

We first derive the two-body dynamics in the non-dimensional form. The equation of motion of the two-body dynamics, in the dimensional form, is

$$\ddot{\vec{r}} = -\frac{GM}{r^3}\vec{r} \tag{2}$$

Now we choose the normalizing distance as R^* and the normalizing speed (V^*) as the orbital speed on a circular orbit at the normalizing radius. Then, the the normalizing time (τ) is obtained by dividing the normalizing distance by the normalizing speed.

$$\vec{\imath} = \frac{\vec{r}}{R^*} \tag{3}$$

$$\vec{\nu} = \frac{\vec{V}}{V^*} \tag{4}$$

$$V^* = \sqrt{\frac{GM}{R^*}} \tag{5}$$

$$\tau = \frac{R^*}{V^*} = \sqrt{\frac{R^{*3}}{GM}} \tag{6}$$

We will denote the non-dimensional spacecraft position and velocity as $\vec{\boldsymbol{\imath}}$ and $\vec{\boldsymbol{\nu}}$. Then, the partial derivative of time t with respect to the normalized time τ is

$$\frac{\partial \tau}{\partial t} = \sqrt{\frac{GM}{R^{*3}}} \tag{7}$$

This means that every second in the real time (t) should be scaled by $\sqrt{GM/R^{*3}}$ in the non-dimensional space. Thus, the partial derivative of time is now transformed to

$$\frac{\partial}{\partial t} = \frac{\partial}{\partial \tau}\frac{\partial \tau}{\partial t} = \frac{\partial}{\partial \tau}\sqrt{\frac{GM}{R^{*3}}} \tag{8}$$

$$\frac{\partial^2}{\partial t^2} = \frac{GM}{R^{*3}}\frac{\partial^2}{\partial \tau^2} \tag{9}$$

Thus, we can rewrite Equation 2 as

$$\frac{\partial^2 \vec{r}}{\partial t^2} = R^*\frac{\partial^2 \vec{\boldsymbol{\imath}}}{\partial t^2} = R^*\frac{GM}{R^{*3}}\frac{\partial^2 \vec{\boldsymbol{\imath}}}{\partial \tau^2} = \frac{GM}{R^{*2}}\frac{\partial^2 \vec{\boldsymbol{\imath}}}{\partial \tau^2} = -\frac{GM}{r^3}\vec{r} = -\frac{GM}{R^{*2}}\frac{1}{\boldsymbol{\imath}^3}\vec{\boldsymbol{\imath}} \tag{10}$$

which yields

$$\frac{\partial^2 \vec{\boldsymbol{\imath}}}{\partial \tau^2} = -\frac{1}{\boldsymbol{\imath}^3}\vec{\boldsymbol{\imath}} \tag{11}$$

Therefore, the non-dimensional equations of motion has the unity GM irrespective of the body. It is convenient to set the normalizing distance as the reference radius of the spherical harmonics in order to simplify the expression for the higher-degree and higher-order terms, as shown below.

B. General Potential and Acceleration Expressions in Non-dimensional Forms

The gravitational potential in Equation 1 has the units of $[km^2/s^2]$. Thus, to non-dimensionalize it, we multiply it by $\tau^2/R^{*2} = R^*/GM$ to get

$$\bar{U} = \sum_{n=0}^{\infty}\sum_{m=0}^{n}\left(\frac{1}{\boldsymbol{\imath}}\right)^{n+1} P_{nm}(\sin\phi)\begin{bmatrix}\cos(m\lambda)\\ \sin(m\lambda)\end{bmatrix}\cdot\begin{bmatrix}C_{nm}\\ S_{nm}\end{bmatrix} \tag{12}$$

$$\frac{\partial^2 \bar{x}}{\partial \tau^2} = \frac{\partial \bar{U}}{\partial \bar{x}} = \sum_{n=0}^{\infty}\sum_{m=0}^{n}\begin{bmatrix}C_{nm}\\ S_{nm}\end{bmatrix}\cdot\left[-\frac{1}{2}(1+\delta_{0,m})b^*_{n+1,m+1} + \frac{1}{2}\frac{(n-m+2)!}{(n-m)!}b^*_{n+1,m-1}\right] \tag{13}$$

$$\frac{\partial^2 \bar{y}}{\partial \tau^2} = \frac{\partial \bar{U}}{\partial \bar{y}} = \sum_{n=0}^{\infty}\sum_{m=0}^{n}\begin{bmatrix}S_{nm}\\ -C_{nm}\end{bmatrix}\cdot\left[\frac{1}{2}(1+\delta_{0,m})b^*_{n+1,m+1} + \frac{1}{2}\frac{(n-m+2)!}{(n-m)!}b^*_{n+1,m-1}\right] \tag{14}$$

$$\frac{\partial^2 \bar{z}}{\partial \tau^2} = \frac{\partial \bar{U}}{\partial \bar{z}} = \sum_{n=0}^{\infty}\sum_{m=0}^{n}\begin{bmatrix}C_{nm}\\ S_{nm}\end{bmatrix}\cdot\left[-(n-m+1)b^*_{n+1,m}\right] \tag{15}$$

where the overbar denotes the non-dimensional quantities and the basis function b^*_{nm} is defined as

$$b^*_{nm} = \left(\frac{1}{\boldsymbol{\imath}}\right)^{n+1} P_{nm}(\sin\phi)\begin{bmatrix}\cos(m\lambda)\\ \sin(m\lambda)\end{bmatrix} \tag{16}$$

Thus, the potential is still a linear combination of the original spherical harmonics, which are already non-dimensional and body specific parameters. If one wishes to work in the *normalized* spherical harmonics,[18] the normalized, non-dimensional equations of motion can be obtained effortlessly by using the normalized parameters for the spherical harmonics and by replacing the basis function b^*_{nm} with its normalized counterpart in Equations 13 through 15.

III. Acceleration due to C_{20} and C_{22}

In this section, we look at some properties of the acceleration due to the second-degree spherical harmonics. Because C_{21}, S_{21}, and S_{22} can be zeroed out when the coordinate frame is aligned with the principal axes of the body,[19] we only deal with C_{20} and C_{22} coefficients.

A. C_{20} Acceleration

The acceleration and its magnitude due to C_{20} (which is the negative of the J_2 coefficient widely used in many applications) are given as

$$\ddot{\vec{r}}_{C_{20}} = \frac{\partial \bar{U}_{C_{20}}}{\partial \vec{r}} = \frac{3}{2}\frac{1}{r^7} C_{20} \begin{bmatrix} \bar{x}\left(r^2 - 5\bar{z}^2\right) \\ \bar{y}\left(r^2 - 5\bar{z}^2\right) \\ \bar{z}\left(3r^2 - 5\bar{z}^2\right) \end{bmatrix} \tag{17}$$

$$\left|\ddot{\vec{r}}_{C_{20}}\right| = \frac{3}{2}\frac{1}{r^4} |C_{20}| \sqrt{5\sin^4\phi - 2\sin^2\phi + 1} \tag{18}$$

which is only the function of the latitude. The argument inside the square root is zero when $\sin^2\phi = (1 \pm 2i)/5$. Thus, $\left|\ddot{\vec{r}}_{C_{20}}\right|$ is never zero for real-valued ϕ. This ensures that no matter where the flyby occurs, the spacecraft is perturbed by the C_{20} acceleration. That is, the Doppler measurement is constantly influenced by the C_{20} acceleration unless its change is orthogonal to the line-of-sight. Now we study the sensitivity of $\left|\ddot{\vec{r}}_{C_{20}}\right|$ to the latitude. The zero-crossings of $\partial\left|\ddot{\vec{r}}_{C_{20}}\right|/\partial\phi$ occurs when

$$\begin{array}{rcccrcc} \sin\phi & = & 0 & \rightarrow & \phi & = & 0^\circ \\ \cos\phi & = & 0 & \rightarrow & \phi & = & \pm 90^\circ \\ 5\sin^2\phi - 1 & = & 0 & \rightarrow & \phi & = & \pm 26.565^\circ \end{array} \tag{19}$$

These conditions show that $\phi = 0^\circ$ is the local maximum, $\phi = \pm 26.565$ are global minima, and $\phi = \pm 90^\circ$ are global maxima (Figure 1(a)). Figure 1(b) shows the angle between the plane perpendicular to nadir (i.e., TN-plane in the RTN coordinate frame) and the C_{20} acceleration. Thus, when the C_{20} acceleration is the strongest, it acts in the direction along the radial direction (i.e., the maximum C_{20} accelerations are aligned with the GM acceleration). As C_{20} is negative for an oblate body, this counters the two-body acceleration. In other words, the oblateness translates to missing mass at the poles.

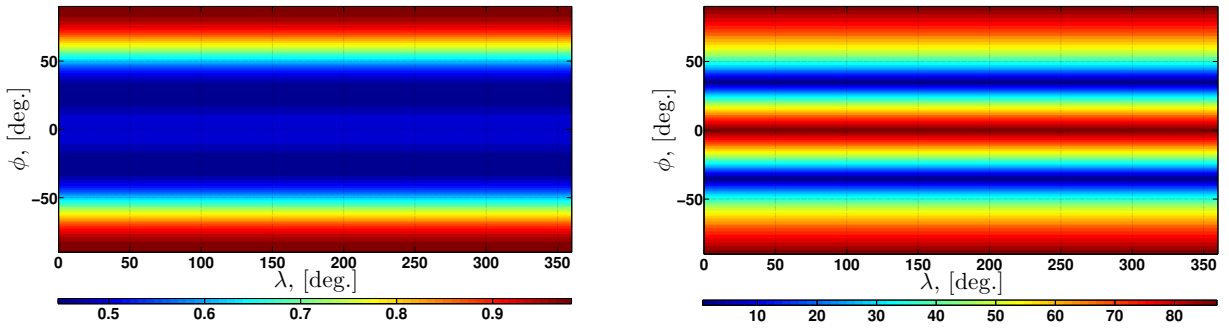

(a) $\left|\ddot{\vec{r}}_{C_{20}}\right|$ normalized by the maximum acceleration

(b) Angular offset (deg.) of $\ddot{\vec{r}}_{C_{20}}$ from the TN-plane

Figure 1. Normalized magnitude of the C_{20} acceleration (i.e., scaled to the maximum value of unity) and its angle from the plane perpendicular to nadir. In the radial, transverse, normal (RTN) frame (also known as radial, in-track, and cross-rack frame), this plane is the TN-plane. That is, the value of 0° indicates that the C_{20} acceleration is perpendicular to the radial vector, and the value of 90° is parallel.

B. C_{22} Acceleration

The C_{22} acceleration is given as follows:

$$\ddot{\vec{r}}_{C_{22}} = \frac{\partial \bar{U}_{C_{22}}}{\partial \vec{r}} = -3\frac{1}{r^7}C_{22}\begin{bmatrix} \bar{x}\left(5\bar{x}^2 - 5\bar{y}^2 - 2r^2\right) \\ \bar{y}\left(5\bar{x}^2 - 5\bar{y}^2 + 2r^2\right) \\ 5\bar{z}(\bar{x}^2 - \bar{y}^2) \end{bmatrix} \tag{20}$$

$$\left|\ddot{\vec{r}}_{C_{22}}\right| = 3\frac{1}{r^4}C_{22}\cos\phi\sqrt{5\cos^2\phi\cos^2 2\lambda + 4} \tag{21}$$

By inspection, $\cos\phi \geq 0$ and the quantity within the square root is larger than zero. The maximum and minimum values of the C_{22} acceleration are given as

$$\left|\ddot{\vec{r}}_{C_{22}}\right|_{max} = \frac{9C_{22}}{r^4} \quad \text{for} \quad \begin{cases} \phi = 0^\circ \\ \lambda = 90^\circ q \text{ where } q = 0, 1, 2, \ldots \end{cases}$$

$$\left|\ddot{\vec{r}}_{C_{22}}\right|_{min} = 0 \quad \text{for} \quad \begin{cases} \phi = \pm 90^\circ \\ \lambda = N.A. \end{cases}$$

Thus, unlike the C_{20} acceleration, the maximum C_{22} does not occur at the poles, but does along the equator (Figure 2(a)). It is also when the acceleration is aligned with the two-body acceleration (Figure 2(b)).

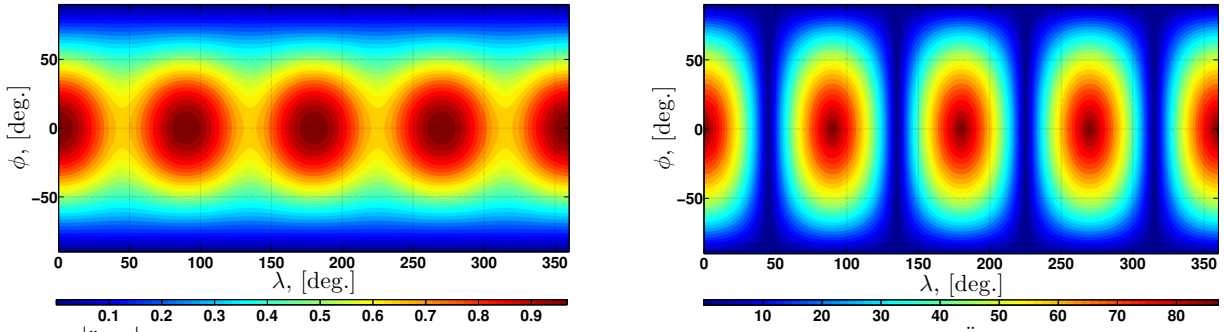

(a) $\left|\ddot{\bar{r}}_{C_{22}}\right|$ normalized by the maximum acceleration

(b) Angular offset (deg.) of $\ddot{\bar{r}}_{C_{22}}$ from the TN-plane

Figure 2. Normalized magnitude of the C_{22} acceleration and its angle from the TN-plane.

IV. Coordinate frames

The covariance of the spacecraft state and other parameters are prescribed in the inertial frame. Anderson[13] defines his coordinate frame such that the origin is at the center of mass of the asteroid, and the inertial z-axis is directed from the asteroid to Earth. The directions of x and y-axes are arbitrary. Thus, for convenience, we orient the inertial xy-plane such that the pole of the body lies in the inertial xz-plane. The flyby orientation is uniquely determined from the 3-1-3 Euler angles: right ascension Ω_A, inclination i_A, and argument of perigee ω_A, where the subscript A is for Anderson. This frame is considered our inertial frame. Then, together with the target radius (b_p, where p is for periapsis) and the target flyby speed (V_p), we can specify the flyby geometry. This coordinate frame has an advantage that the first rotation about the z-axis does not play a role when computing Doppler due to GM (Section VII).

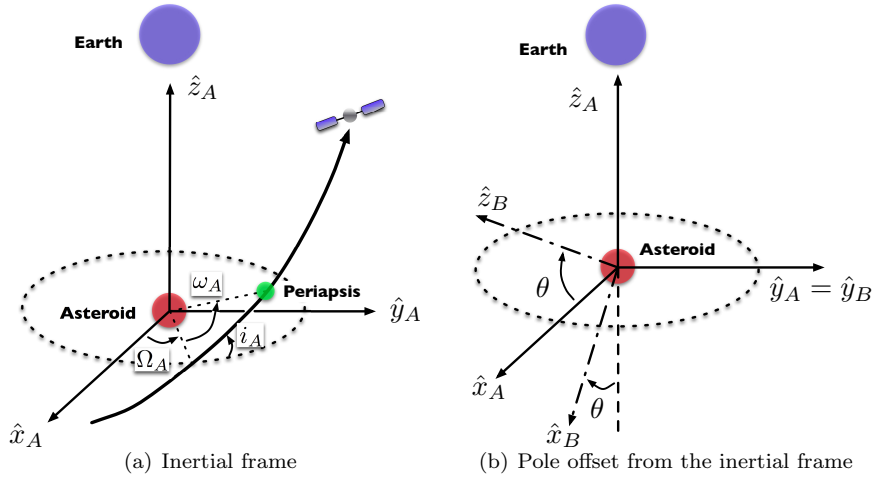

(a) Inertial frame

(b) Pole offset from the inertial frame

Figure 3. Coordinate frames.

Note that while the covariance output is needed in the inertial frame, the higher-degree and higher-order gravitational terms must be computed in the asteroid body frame (B subscript). For a principal axis rotator, the body frame is uniquely defined by specifying the pole orientation, the rotation rate, and the reference time. We assume that the nominal pole orientation ($\hat{z}_B$ axis) is along $\hat{x}_A$, the body is uniformly rotating at $\dot{\omega}_{Rot} = 2\pi/T$ where T is the rotation period, and the reference time is the passage of periapsis. The rotation period in the non-dimensional space is denoted as $\bar{T}$. In order to model a body with a different pole orientation, we define the angular offset of the pole (θ) in the inertial xz-plane. That is, the pole offset is angle between $\hat{x}_A$ and $\hat{z}_B$, measured positive in the clockwise direction around the y-axis. Due to the symmetry around $\hat{z}_A$, only θ is necessary to specify the orientation of the pole. The time of passage can also

be altered by defining another reference time, but we do not study its effect in this paper.

V. Doppler Measurement

Doppler is the primary radiometric data used in all spacecraft missions. In this section, we investigate what information content Doppler contains for GM, C_{20}, and C_{22} harmonic coefficients. For convenience, we derive the equations in the dimensional space.

Doppler measurement is the velocity change along the line-of-sight from the Earth to the spacecraft ($\hat{\varrho}$). Equations 22 through 24 show the Doppler due to GM, C_{20}, and C_{22}:

$$\Delta V_{GM}^{Dop}(t_k) = \int_{t_0}^{t_k} (\vec{a}_{GM} \cdot \hat{\varrho})\, dt \tag{22}$$

$$\Delta V_{C_{20}}^{Dop}(t_k) = \int_{t_0}^{t_k} (\vec{a}_{C_{20}} \cdot \hat{\varrho})\, dt \tag{23}$$

$$\Delta V_{C_{22}}^{Dop}(t_k) = \int_{t_0}^{t_k} (\vec{a}_{C_{22}} \cdot \hat{\varrho})\, dt \tag{24}$$

where $\vec{a}$ is the acceleration and the subscript indicates the acceleration due only to that coefficient. In a least-squares filter, the information about the parameters are accumulated via observations and dynamics (i.e., state transition matrix). Therefore, in order to perform covariance analysis, we need to construct a measurement model and the equations of motion. Equation 25 defines our observable model for Doppler:

$$Z_{Dop} = \hat{\varrho} \cdot \vec{V}_{sat} = \left(\frac{\vec{r}_{sat} - \vec{r}_{earth}}{|\vec{r}_{sat} - \vec{r}_{earth}|} \right) \cdot \vec{V}_{sat} \tag{25}$$

where Z denotes the observable. For simplicity, the Earth ground station coordinates are equated to the Earth's ephemeris in the inertial frame, and we ignore the atmospheric calibrations. The measurement model in Equation 25 is the aggregate sum of GM, C_{20}, and C_{22} contributions. If the filter used to estimate these parameters can separate their contributions, we would then be able to obtain a *clean* estimate that is free of corruption from the correlation terms.

The computation of the sensitivity matrix (i.e., observation partial) demonstrates the strength of the observables with respect to the estimated parameters. For example, the sensitivity value of zero means that there is no direct information about the state parameter that can be extracted from the measurement, and the state parameter must be related to the measurement via the state transition matrix (STM, Φ). Let us assume that we want to estimate the position, velocity, GM, and the lower-degree harmonics in the filter. Then, the state vector is defined as

$$\vec{X} = \begin{bmatrix} \vec{r}_{sat} & \vec{V}_{sat} & GM & C_{20} & C_{22} \end{bmatrix} \tag{26}$$

The observable equation (Equation 25) is used to compute the sensitivity matrix ($\tilde{H}$) for the position and velocity of the spacecraft, GM, C_{20}, and C_{22} as follows:

$$\tilde{H}_{Dop} = \frac{\partial Z_{Dop}}{\partial \vec{X}} = \left[\left(1_{[3\times3]} - \hat{\varrho}\hat{\varrho}\right) \cdot \frac{\vec{V}_{sat}}{\varrho}_{[1\times3]}, \quad \hat{\varrho}_{[1\times3]}, \mathbf{0}_{1\times3} \right] \tag{27}$$

Equation 27 is used to accumulate the information matrix (Λ) after being mapped to epoch by the STM. Now, remember that we chose our $\hat{z}_A$ to be directed from the asteroid to the Earth (Section IV). Thus, $\hat{\varrho}$ is approximated as $\hat{\varrho} \approx -\hat{z}_A = [0, 0, -1]$. Also, $\varrho \gg |\vec{V}_{sat}|$. Consequently, Equation 27 becomes

$$\tilde{H}_{Dop} \approx \left[\frac{1}{\varrho} [V_x, V_y, 0], \quad [0, 0, -1], \quad \mathbf{0}_{1\times3} \right] \approx \left[\mathbf{0}_{1\times3}, \quad [0, 0, -1], \quad \mathbf{0}_{1\times3} \right] \tag{28}$$

Then, by direct computation, the sensitivity matrix mapped to epoch (i.e., $H = \tilde{H}\Phi$) is expressed as

$$H(t_k, t_0) \approx -\left[\frac{\partial \dot{z}_k}{\partial x_0} \quad \frac{\partial \dot{z}_k}{\partial y_0} \quad \frac{\partial \dot{z}_k}{\partial z_0} \quad \frac{\partial \dot{z}_k}{\partial \dot{x}_0} \quad \frac{\partial \dot{z}_k}{\partial \dot{y}_0} \quad \frac{\partial \dot{z}_k}{\partial \dot{z}_0} \quad \frac{\partial \dot{z}_k}{\partial GM} \quad \frac{\partial \dot{z}_k}{\partial C_{20}} \quad \frac{\partial \dot{z}_k}{\partial C_{22}}\right] \tag{29}$$

where the STM is defined as

$$\Phi(t_k, t_0) = \begin{bmatrix} \frac{\partial \vec{r}_k}{\partial \vec{r}_0} & \frac{\partial \vec{r}_k}{\partial \vec{V}_0} & \frac{\partial \vec{r}_k}{\partial GM} & \frac{\partial \vec{r}_k}{\partial C_{20}} & \frac{\partial \vec{r}_k}{\partial C_{22}} \\ \frac{\partial \vec{V}_k}{\partial \vec{r}_0} & \frac{\partial \vec{V}_k}{\partial \vec{V}_0} & \frac{\partial \vec{V}_k}{\partial GM} & \frac{\partial \vec{V}_k}{\partial C_{20}} & \frac{\partial \vec{V}_k}{\partial C_{22}} \\ \mathbf{0}_{3\times 6} & & & \mathbf{1}_{3\times 3} & \end{bmatrix} \tag{30}$$

As expected, the information of Doppler resides in the velocity change along the Earth - asteroid direction. Equation 29 is used to construct the information matrix Λ as

$$\Lambda_{Dop} = \sum_{k=0}^{N} \Lambda_k + \bar{P}_0^{-1} = \sum_{k=0}^{N} H_k^T W_{Dop} H_k + \bar{P}_0^{-1} = \frac{1}{\sigma_{Dop}^2} \sum_{k=0}^{N} H_k^T H_k + \bar{P}_0^{-1} \tag{31}$$

where N is the total number of observations, W_{Dop} is the weight matrix, σ_{Dop} is the measurement uncertainty for Doppler at 0.1 $[mm/s]$, and P is the covariance. $\bar{P}_0$ denotes the *a priori* covariance at epoch. The frequency of the Doppler measurement is every 60 $[s]$ and last ± 4 $[hours]$ around the closest approach. Now, by direct expansion of the equation of motion of STM, we get

$$\frac{\partial \vec{V}_k}{\partial GM} = \int_{t_0}^{t_k} \left(\frac{\partial \vec{a}}{\partial \vec{r}} \frac{\partial \vec{r}}{\partial GM} + \frac{\partial \vec{a}}{\partial GM} \right) dt \tag{32}$$

$$\frac{\partial \vec{V}_k}{\partial C_{20}} = \int_{t_0}^{t_k} \left(\frac{\partial \vec{a}}{\partial \vec{r}} \frac{\partial \vec{r}}{\partial C_{20}} + \frac{\partial \vec{a}}{\partial C_{20}} \right) dt \tag{33}$$

$$\frac{\partial \vec{V}_k}{\partial C_{22}} = \int_{t_0}^{t_k} \left(\frac{\partial \vec{a}}{\partial \vec{r}} \frac{\partial \vec{r}}{\partial C_{22}} + \frac{\partial \vec{a}}{\partial C_{22}} \right) dt \tag{34}$$

For a relatively fast (but slow in the absolute sense) flyby around a small body, the magnitudes of the first terms are low compared to the second terms. In other words, the sensitivity of the spacecraft position to the gravitational coefficients are far lower than the spacecraft velocity. Thus, we can ignore the first terms in the integrand in Equation 32 through 34 to approximate Equation 29 as

$$\hat{\varrho} \cdot \frac{\partial \vec{V}_k}{\partial GM} \approx \hat{\varrho} \cdot \int_{t_0}^{t_k} \frac{\partial \vec{a}}{\partial GM} dt = \frac{\Delta V_{GM}^{Dop}(t_k)}{GM} \tag{35}$$

$$\hat{\varrho} \cdot \frac{\partial \vec{V}_k}{\partial C_{20}} \approx \hat{\varrho} \cdot \int_{t_0}^{t_k} \frac{\partial \vec{a}}{\partial C_{20}} dt = \frac{\Delta V_{C_{20}}^{Dop}(t_k)}{C_{20}} \tag{36}$$

$$\hat{\varrho} \cdot \frac{\partial \vec{V}_k}{\partial C_{22}} \approx \hat{\varrho} \cdot \int_{t_0}^{t_k} \frac{\partial \vec{a}}{\partial C_{22}} dt = \frac{\Delta V_{C_{22}}^{Dop}(t_k)}{C_{22}} \tag{37}$$

Thus, the information matrix in Equation 31 can be approximated by

$$\Lambda_k = \begin{bmatrix} \Gamma(GM,GM) & \Gamma(GM,C_{20}) & \Gamma(GM,C_{22}) \\ \Gamma(C_{20},GM) & \Gamma(C_{20},C_{20}) & \Gamma(C_{20},C_{22}) \\ \Gamma(C_{22},GM) & \Gamma(C_{22},C_{20}) & \Gamma(C_{22},C_{22}) \end{bmatrix} \tag{38}$$

where Γ, for parameters c_1 and c_2, is a scalar quantity defined as

$$\Gamma(c_1,c_2) = \Gamma(c_2,c_1) = \frac{1}{\sigma_{Dop}^2}\sum_{k=0}^{N}\frac{\Delta V_{c_1}^{Dop}(t_k)\Delta V_{c_2}^{Dop}(t_k)}{c_1 c_2} + \bar{P}_0^{-1}(c_1,c_2) \tag{39}$$

Γ can be used as the proxy for the information matrix and the full numerical filter is not necessary to obtain the rough performance of the covariance analysis (Figure 4). This cuts down the computation time immensely since running the full filter for a large number of different conditions is expensive. Zero correlation occurs when $\Delta V_{c_1}^{Dop}(t_k)$ is along $\hat{\varrho}$ and $\Delta V_{c_2}^{Dop}(t_k)$ is perpendicular to $\hat{\varrho}$, and vice versa. However, it is extremely hard to de-correlate the gravitational coefficients, much more so when there are correlations with position and velocity of the spacecraft. One way to address this problem is to work in the ideal situation where we only estimate one gravitational coefficient at a time. Such scenario would assume that the spacecraft position/velocity are well known, and each flyby attempt to reduce the uncertainty for only one gravitational coefficient such that all information content is directly applied to solve for that particular parameter.

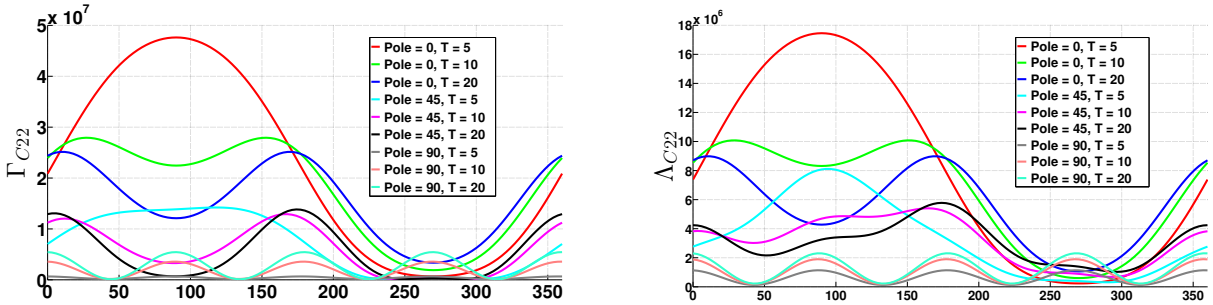

(a) $\Gamma_{C_{22},C_{22}}$ (b) $\Lambda_{C_{22},C_{22}}$

Figure 4. $\Gamma_{C_{22},C_{22}}$ and $\Lambda_{C_{22},C_{22}}$. The gravity field is that of Bennu. $\bar{b}_p = 2.03$ and $\bar{V}_p = 3.874$ (i.e., non-dimensional target radius and target flyby speed). The pole offset (θ) is varied from $0°$, $45°$, to $90°$. The rotation period in the non-dimensional space is 5, 10, and 20. That is, $T = 5\tau$, 10τ, and 20τ. The inclination and the argument of perigee are fixed at $i_A = 90°$ and $\omega_A = 90°$. The right ascension is varied from $0°$ to $360°$. It is shown that the Doppler proxy (Γ) approximates the behavior of the full information (Λ) well, except for the magnitude. The magnitude of the information is of lesser importance since the information of GM and C_{20} scales similarly.

VI. Optical Navigation

The observation model for optical navigation (OpNav) is simply the line-of-sight vector from the spacecraft to the landmarks on the asteroid surface in the asteroid body frame.

$$Z_{Opn} = -\hat{r}_B = -[BA]\left(\frac{\vec{r}_{sat}-\vec{r}_{ast}}{|\vec{r}_{sat}-\vec{r}_{ast}|}\right) = -[BA]\hat{r}_N \tag{40}$$

where the rotation matrix $[BA]$ maps a vector in the inertial frame (A) into the body frame (B). Then, the partial of Equation 40 with respect to the spacecraft position/velocity is given as

$$\tilde{H}_{Opn} = \frac{\partial Z_{Opn}}{\partial\left(\vec{r}_{sat}, \vec{V}_{sat}\right)} = \left[-\frac{1}{r}[BA]\left(1_{[3\times3]} - \hat{r}_A\hat{r}_A\right), \quad 0_{[3\times3]} \right] = \left[\tilde{H}_{1,Opn}, \quad 0_{[3\times3]} \right] \tag{41}$$

$$H_{Opn}(t_k, t_0) = \left[\tilde{H}_{1,Opn}\frac{\partial\vec{r}_k}{\partial\vec{r}_0} \quad \tilde{H}_{1,Opn}\frac{\partial\vec{r}_k}{\partial\vec{V}_0} \quad \tilde{H}_{1,Opn}\frac{\partial\vec{r}_k}{\partial GM} \quad \tilde{H}_{1,Opn}\frac{\partial\vec{r}_k}{\partial C_{20}} \quad \tilde{H}_{1,Opn}\frac{\partial\vec{r}_k}{\partial C_{22}}\right] \tag{42}$$

Thus, OpNav's information content is in the sensitivity of the spacecraft position with respect to the estimated parameters, where as Doppler's information content is in that of the spacecraft velocity with respect to the estimated parameters.

The weight matrix of OpNav is provided in the RTN frame. That is, its uncertainty is with respect to the viewing geometry of the spacecraft relative to the body. We denote the rotation matrix from the RTN frame (R) to the inertial frame (A) as [AR], and the reverse direction as [RA]. Then, the weight matrix in the RTN frame (W_{RTN}^{Opn}) is converted into that in the inertial frame (W_A^{Opn}) as

$$W_A^{Opn} = [AR]W_{RTN}^{Opn}[RA] \tag{43}$$

where

$$W_{RTN}^{Opn} = \begin{bmatrix} 0 & 0 & 0 \\ 0 & \dfrac{1}{\sigma_{Opnav}^2} & 0 \\ 0 & 0 & \dfrac{1}{\sigma_{Opnav}^2} \end{bmatrix} \tag{44}$$

Equation 44 shows that the OpNav measures the direction but not the distance. Thus, there is no information content along the radial direction from a single OpNav observation. The direction is specified by two angles (azimuth and elevation), and the OpNav gives two rank of information while each Doppler adds only one rank of information. For example, suppose that the $\hat{r}_A$ points along the x-axis. Then, the first element of $\left(1_{[3\times3]} - \hat{r}_A\hat{r}_A\right)$ is zero in Equation 41 and the information in this direction is not existent. The camera model that we use is field-of-view (FOV) of 10° with 1024 pixels, and we assume that we can resolve the image to 0.5 pixel, which gives $\sigma_{Opnav} = 8.52 \times 10^{-5}$ $[rad.]$. It is assumed that an OpNav data is taken every 30 minutes for ± 4 $[hours]$ around the closest approach, and there are two landmarks in each picture that are diametrically opposite on the limb. We do not consider the lighting conditions, so the landmarks are always visible.

VII. GM Estimation

The analysis by Anderson[13] shows that GM is best estimated when the inclination is at 90° and the argument of perigee is 30°. However, Sybert et al.[14] formulates the GM uncertainty in terms of the orbit energy and turn angle and reveals that the GM uncertainty is better obtained when the viewing angle is such that the spacecraft transits in front of the body. This case yields the uncertainty that is half of when the viewing angle is parallel to the spacecraft velocity. Comparing the two analyses, Sybert's result makes more intuitive sense since maximum Doppler change is recorded when the spacecraft velocity changes along the Earth - spacecraft line-of-sight direction. This discrepancy is thought to arise from Anderson's formulation where the GM estimate is correlated with the flyby geometry. Without this correlation, the maximum information content is indeed obtained at the argument of perigee of 90° (Figure 5).

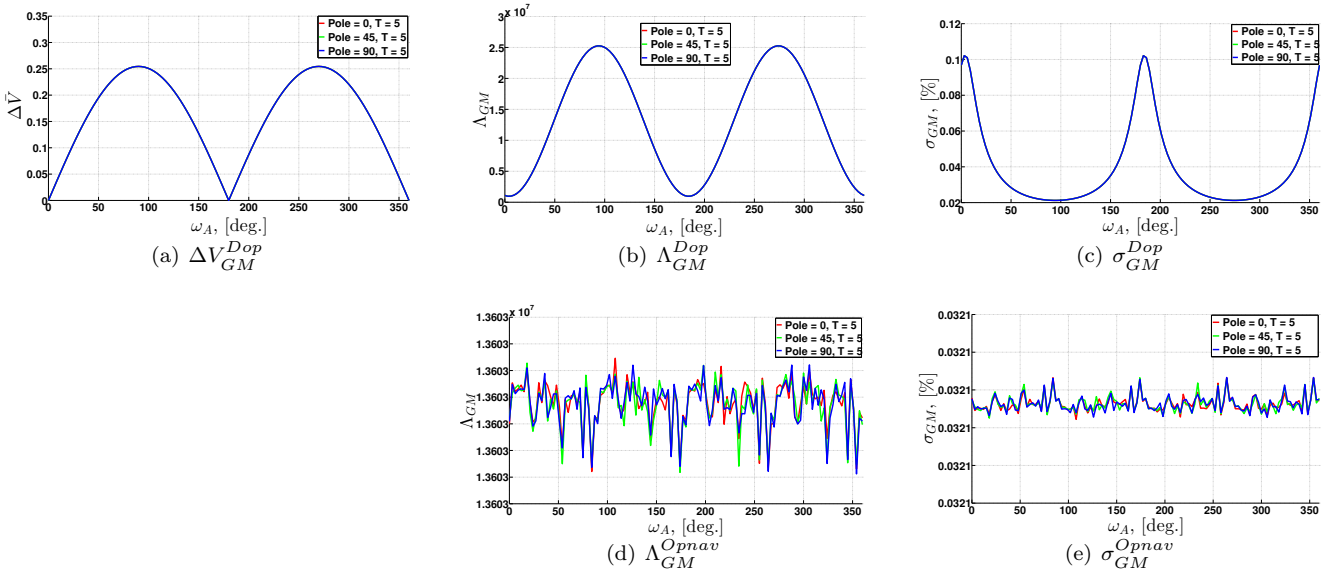

(a) ΔV_{GM}^{Dop} (b) Λ_{GM}^{Dop} (c) σ_{GM}^{Dop}

(d) Λ_{GM}^{Opnav} (e) σ_{GM}^{Opnav}

Figure 5. Doppler change and GM information/covariance as a function of ω_A for a fixed inclination $i_A = 90°$. $\bar{b}_p = 2.03$ and $\bar{V}_p = 3.874$. The right ascension does not play a role when only the GM is estimated. The pole angle offsets of $0°$, $45°$, and $90°$ are tested for the rotation period of $\bar{T} = 5$. The information and covariance by Doppler and OpNav do not change with pole offset/rotation period, because there is only two-body acceleration.

As expected, OpNav (Figures 5(d) and 5(e)) yields the same information/uncertainty irrespective of the argument of perigee because the relative geometry is the same for this measurement. Thus, this result shows that when science requires that the periapsis occurs near the xy-plane (i.e., small component along $\hat{z}_A$) in the inertial frame, OpNav is a more reliable measurement than Doppler.

VIII. C_{20} and C_{22} Estimation

In this section, we evaluate the performance of C_{20} and C_{22} covariance for numerous flyby geometries. Section VII showed that GM is best determined when $i_A = 90°$ and $\omega_A = 90°$, regardless of the right ascension. However, because the C_{20} and C_{22} accelerations are computed in the body frame, it is not analytically trivial to find a combination of the inclination, argument of perigee, and right ascension that yields the minimum uncertainties for these coefficients. Thus, we performed the exhaustive search for the minimum covariance value around Bennu[20] and Itokawa.[21] Their gravity field parameters are listed in Table 1. Bennu's gravity field is constructed from the uniform density, and the actual density value is irrelevant since we will be using the non-dimensional dynamics presented in Section II. The resolution of the grid search is $30°$ for inclination and $10°$ for argument of perigee and right ascension. For both bodies, $\bar{b}_p = 2.03$ and $\bar{V}_p = 3.874$. The pole offsets and the rotation periods are varied. Table 2 shows where the minimum covariance for GM, C_{20}, and C_{22} occurred when only Doppler is processed.

Table 1. Reference radius, GM, C_{20}, and C_{22} for Bennu.

Body	R^* [km]	GM $[km^3/s^2]$	C_{20}	C_{22}
Bennu	0.2465	4.1062×10^{-9}	-3.4264×10^{-2}	3.4483×10^{-3}
Itokawa	0.1619	2.36×10^{-9}	-0.3247	0.1416

Table 2. Inclination, argument of perigee, and right ascension for the minimum GM, C_{20}, and C_{22} uncertainties with Doppler. Bennu and Itokawa are the target bodies.

	θ, [deg.]	$\bar{T}$, [n.d.]	i_{Ben}, [deg]	ω_{Ben}, [deg]	Ω_{Ben}, [deg]	i_{Ito}, [deg]	ω_{Ito}, [deg]	Ω_{Ito}, [deg]
GM	–	–	270	270	130	270	270	40
C_{20}	0	5	210	270	90	30	90	270
	0	10	30	90	270	330	270	90
	0	20	330	270	90	150	90	270
	45	5	180	330	330	180	170	350
	45	10	180	160	160	180	90	270
	45	20	0	320	40	180	80	260
	90	5	150	90	340	30	90	190
	90	10	150	90	70	30	90	190
	90	20	30	90	290	330	270	0
C_{22}	0	5	90	270	90	90	270	90
	0	10	90	90	150	90	90	120
	0	20	150	70	160	90	90	20
	45	5	60	270	90	60	270	90
	45	10	30	270	0	60	90	90
	45	20	30	290	350	30	280	350
	90	5	30	270	0	330	90	0
	90	10	330	270	180	30	90	0
	90	20	330	270	180	330	270	0

The result shows that GM is best estimated when the inclination and the argument of perigee are either 90° or 270° (equivalent in terms of the Doppler shift). Comparing numbers, it is seen that there are a lot of similarities where the minimum uncertainty occurs for the inclination, argument of perigee, and right ascension. There are angles that are separated by 180° and by the same angle around a reference angle (i.e., $X \pm \Delta$ [deg.]). The following tables show the longitude (λ) and latitude (ϕ) of the target point in the body frame, and the angle (β) between the periapsis velocity and the transverse axis $\hat{\mathscr{T}}$ obtained by

$$\hat{\mathscr{T}} = \frac{\hat{z}_B \times \vec{\boldsymbol{r}}_B}{|\hat{z}_B \times \vec{\boldsymbol{r}}_B|} \tag{45}$$

That is, the angle β can be comprehended as the rise angle of the periapsis velocity.

Table 3. Longitude (λ) and latitude (ϕ) of the target point in the body frame and the rise angle (β) for the minimum GM, C_{20}, and C_{22} uncertainties with Doppler for Bennu and Itokawa.

	θ, [deg.]	$\bar{T}$, [n.d.]	λ_{Ben}, [deg]	ϕ_{Ben}, [deg]	β_{Ben}, [deg]	λ_{Ito}, [deg]	ϕ_{Ito}, [deg]	β_{Ito}, [deg]
GM	–	–	−180.00	−0.00	140.00	180.00	−0.00	130.00
C_{20}	0	5	−180.00	−60.00	180.00	−180.00	60.00	180.00
	0	10	−180.00	60.00	180.00	−180.00	60.00	180.00
	0	20	−180.00	60.00	180.00	180.00	−60.00	180.00
	45	5	0.00	45.00	180.00	180.00	−45.00	180.00
	45	10	0.00	45.00	180.00	180.00	−45.00	180.00
	45	20	−0.00	45.00	0.00	−180.00	−45.00	180.00
	90	5	−110.00	30.00	180.00	−80.00	30.00	0.00
	90	10	−20.00	30.00	180.00	−80.00	30.00	0.00
	90	20	20.00	30.00	0.00	−90.00	30.00	0.00
C_{22}	0	5	−0.00	0.00	0.00	−0.00	0.00	0.00
	0	10	−180.00	−0.00	60.00	180.00	−0.00	30.00
	0	20	118.05	−2.46	80.14	180.00	0.00	70.00
	45	5	−0.00	−15.00	0.00	−0.00	−15.00	0.00
	45	10	−67.79	−20.70	49.10	180.00	15.00	0.00
	45	20	−61.34	−11.18	55.83	−67.27	−19.38	54.26
	90	5	−90.00	−30.00	0.00	90.00	−30.00	0.00
	90	10	90.00	30.00	0.00	90.00	30.00	0.00
	90	20	90.00	30.00	0.00	−90.00	30.00	0.00

From Table 3, one can extract some important characteristics. First, the rotation rate does not play a role when estimating C_{20}. This is because the C_{20} acceleration is only a function of the latitude (Equation 18). As long as the latitudinal coverage is identical for a given observing geometry, the covariance value is the same. Also, note that the angle β is parallel to the transverse axis for all cases. This means that the maximum latitude is attained at the periapsis and almost symmetric coverage of the latitudes is accomplished save for the rotation of the body. For C_{22}, there does not appear to be a good correlation between the longitude and latitude. However, β increases as the rotation rate is decreased (i.e., higher $\bar{T}$), except when $\theta = 90°$. This is because of the longitudinal dependency in Equation 21. The spacecraft attempts to stay as close to the same longitude as it can to feel the consistent tug by the C_{22} acceleration, which makes the spacecraft cut along the north-south direction when the rotation rate is slower.

Figure 6 shows the contour plot of the GM, C_{20}, and C_{22} uncertainties in percentage of the value with respect to the target radius and target velocity for the optimal flyby geometry shown in Table 2. Due to limited spacing, we only show the contour plots for Bennu.

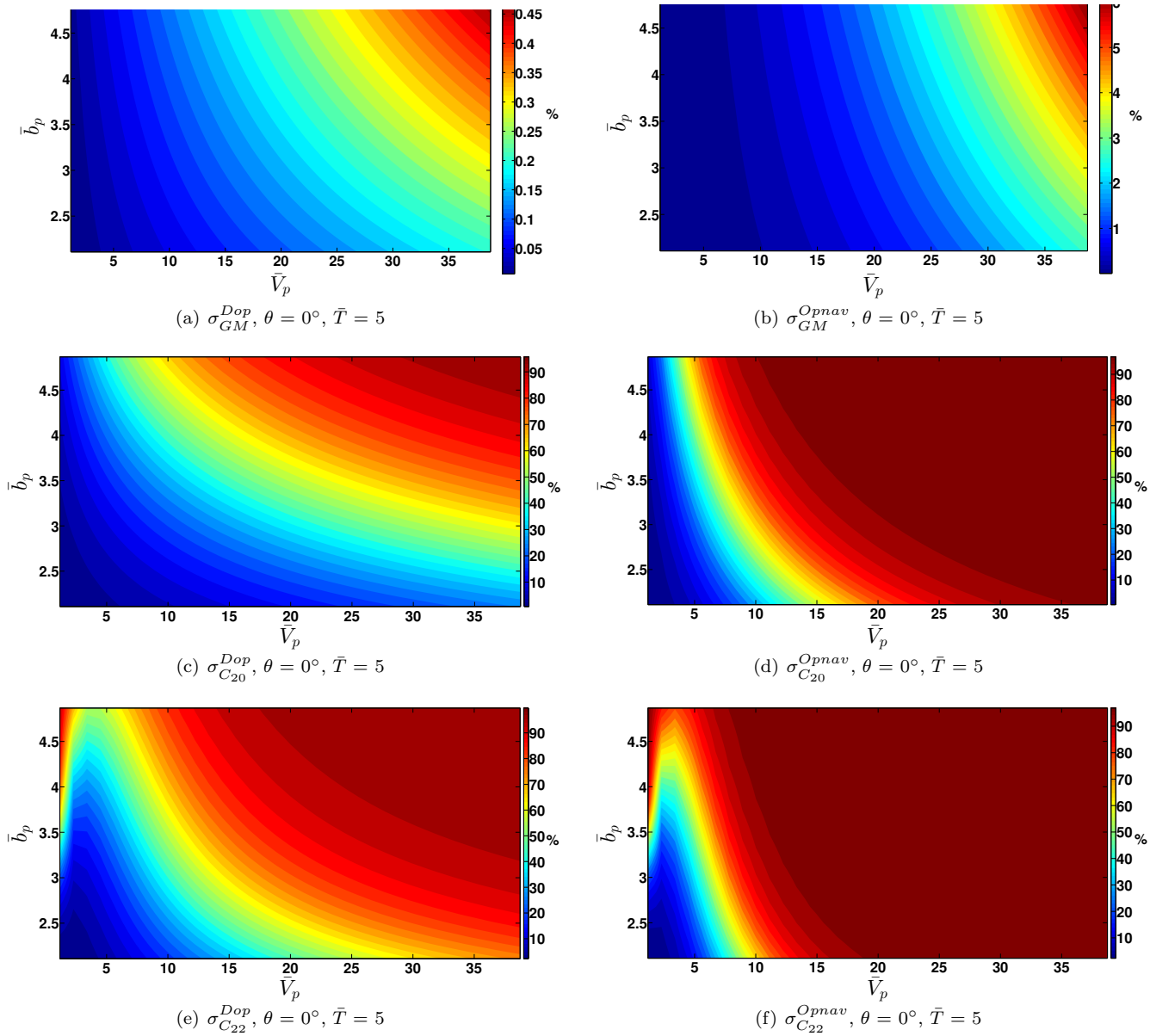

(a) σ_{GM}^{Dop}, $\theta = 0°$, $\bar{T} = 5$

(b) σ_{GM}^{Opnav}, $\theta = 0°$, $\bar{T} = 5$

(c) $\sigma_{C_{20}}^{Dop}$, $\theta = 0°$, $\bar{T} = 5$

(d) $\sigma_{C_{20}}^{Opnav}$, $\theta = 0°$, $\bar{T} = 5$

(e) $\sigma_{C_{22}}^{Dop}$, $\theta = 0°$, $\bar{T} = 5$

(f) $\sigma_{C_{22}}^{Opnav}$, $\theta = 0°$, $\bar{T} = 5$

Figure 6. Contour of GM, C_{20}, and C_{22} uncertainties (% of the value) as functions of $\bar{b}_p$ and $\bar{V}_p$ for Bennu. The pole offset is $0°$, and the normalized rotation period is 5. i_A, ω_A, and Ω_A are configured so that they yield the minimum uncertainty for both coefficients when $\bar{b}_p = 2.03$ and $\bar{V}_p = 3.874$ (Table 2).

The above contour plot defines the best possible uncertainty for a given gravity field and observing geometry. This is because we only estimate one parameter at a time, leveraging all the information available from the observations. However, the general trend of the uncertainties as a function of $\bar{b}_p$ and $\bar{V}_p$ is very similar for other bodies, which is a merit of using the non-dimensional coordinates. One interesting feature that we can observe in Figure 7 is that the C_{22} uncertainties have spikes that do not exist in the C_{20} uncertainties. These are due to the rotation of the body, and we plotted the C_{22} uncertainties due to Doppler for various rotation periods in Figure 7.

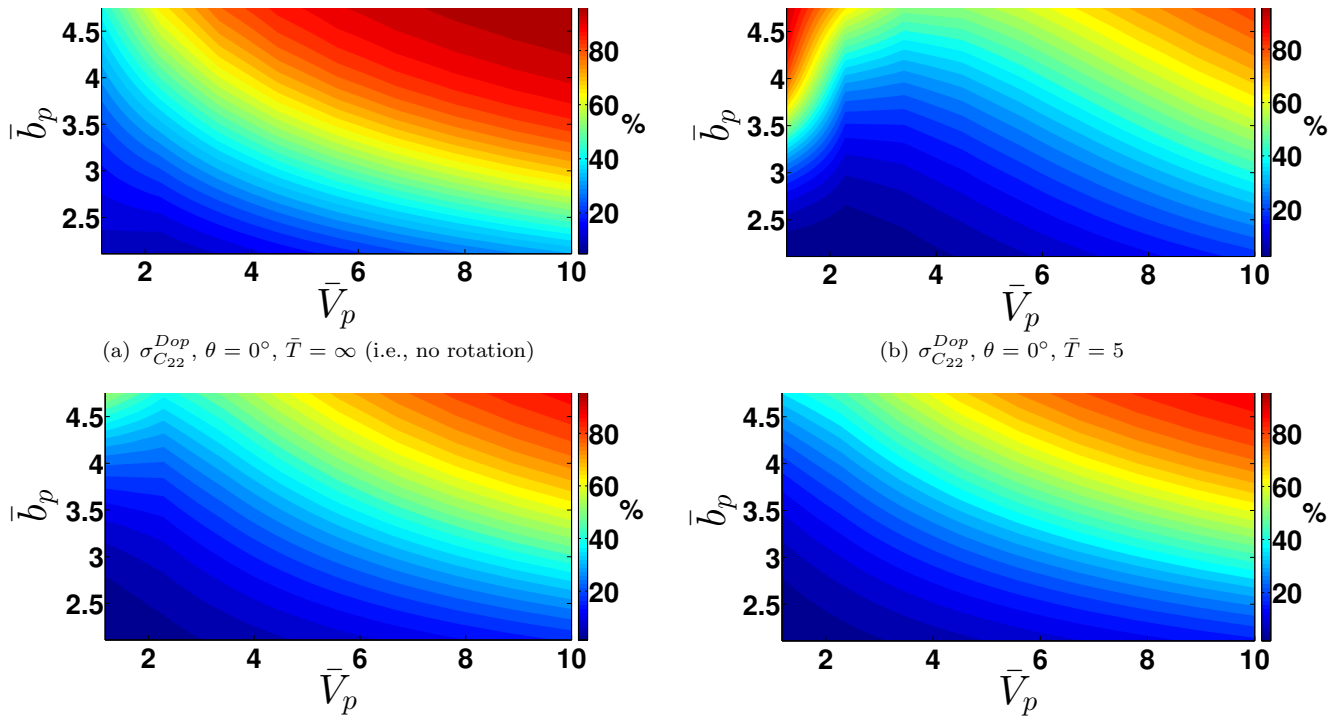

(a) $\sigma_{C_{22}}^{Dop}$, $\theta = 0°$, $\bar{T} = \infty$ (i.e., no rotation)

(b) $\sigma_{C_{22}}^{Dop}$, $\theta = 0°$, $\bar{T} = 5$

(c) $\sigma_{C_{22}}^{Opnav}$, $\theta = 0°$, $\bar{T} = 10$

(d) $\sigma_{C_{22}}^{Opnav}$, $\theta = 0°$, $\bar{T} = 20$

Figure 7. Doppler C_{22} uncertainties (% of the value) as functions of $\bar{b}_p$ and $\bar{V}_p$ for Bennu for different rotation periods. Note that the range of $\bar{V}_p$ is different from Figure 6. The pole offset is $0°$ for all cases. i_A, ω_A, and Ω_A are configured so that they yield the minimum uncertainty for both coefficients when $\bar{b}_p = 2.03$ and $\bar{V}_p = 3.874$ (Table 2). This plot shows that the cause of the peaks in the contour are due to the rotation of the body.

Now, we realize that the flyby geometry given in Table 3 is only for the particular set of target radius and target speed. Therefore, it is important to check if the magnitude of uncertainty in Figure 6 is consistent for different sets of optimal flyby geometry given by another set of target radius and target speed. For this purpose Figure 8 is generated for Bennu. First, we choose a pair of $\bar{b}_p$ and $\bar{V}_p$ in Figure 6(c) for C_{20} and another in Figure 6(e) for C_{22}. Specifically, we chose $\bar{b}_p = 3.3$ and $\bar{V}_p = 20$ for C_{20} and $\bar{b}_p = 4.5$ and $\bar{V}_p = 2.287$ for C_{22}, both of which yield $\sim 50\%$ uncertainty. For both cases, the pole offset is $0°$ and $\bar{T} = 5$. Then, for these target radii and target speeds, we perform the exhaustive search to find the geometry that yields the global minimum for their uncertainties. We found that such cases exist when $i_A = 150°$ for C_{20} and $i_A = 270°$ for C_{22}. The contour plot of their uncertainties with respect to ω_A and Ω_A are generated for those inclinations (Figure 8). Then, as shown, the minimum uncertainty is about the same order of magnitude around 50%, indicating that the magnitude of the uncertainties given in Figure 6 are consistent.

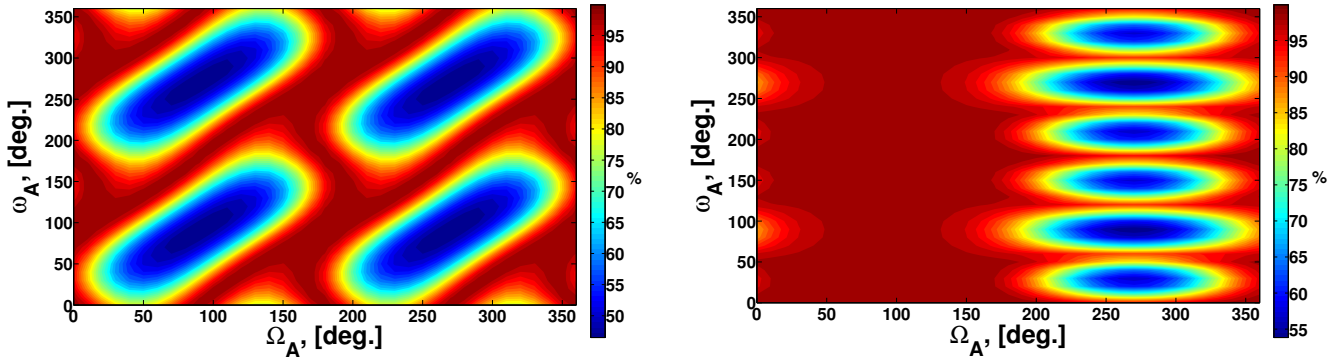

(a) $\sigma_{C_{20}}^{Dop}$ with $i_A = 150°$, $\bar{b}_p = 3.3$ and $\bar{V}_p = 20$

(b) $\sigma_{C_{22}}^{Dop}$ with $i_A = 270°$, $\bar{b}_p = 4.5$ and $\bar{V}_p = 2.287$

Figure 8. Contour of C_{20} and C_{22} uncertainties (% of the value) as functions of $\bar{b}_p$ and $\bar{V}_p$ for Bennu. $\theta = 0°$, $\bar{T} = 5$. $\bar{b}_p = 3.3$ and $\bar{V}_p = 20$ is used to find the combination of i_A, ω_A, and Ω_A that yields the minimum uncertainty for C_{20}, and $\bar{b}_p = 4.5$ and $\bar{V}_p = 2.287$ for C_{22}. The exhaustive search shows that $i_A = 150°$ yields such a case for C_{20} and $i_A = 270°$ for C_{22}.

IX. Conclusion

This paper investigated the covariance analysis of the gravitational parameter and the second-degree spherical harmonic coefficients around small bodies. The equations of motion are non-dimensionalized so the GM is unity. The gravitational field is then independent of the gravitational parameter (i.e., mass/size) and simply a function of the combination of the higher-degree and higher-order coefficients. The force model only contains the gravitation from the small body and ignores other perturbations such as solar radiation pressure to isolate the estimation performance of the lower-degree gravitational parameters.

Following the derivation of the non-dimensional dynamics, we studied the properties of the C_{20} and C_{22} accelerations to show where the maximum/minimum accelerations occur as well as their angle from the point-mass acceleration. We showed that the C_{20} is independent of longitude and is maximum at the poles and minimum at $\phi = 26.5°$. C_{22} acceleration is minimum at the poles (its magnitude is zero) and maximum along equator separated by 90°.

We then proceeded to define the coordinate frames, where the inertial z-axis is directed from the asteroid to Earth and the body pole is in the xz-plane. This coordinate frame has an advantage that Doppler due to GM is independent of the right ascension. In addition, due to symmetry, the pole orientation is specified by only one quantity, namely the pole offset θ. This coordinate frame conveniently allows one to specify the flyby geometry by widely used 3-1-3 Euler angles that are right ascension, inclination, and argument of perigee.

In order to develop a least-squares filter, the observation models are constructed for Doppler and optical navigation (OpNav). It is shown that Doppler's information resides in the line-of-sight velocity perturbation and OpNav's information in the position perturbation due to the gravity. A simplification in Doppler formulation allows one to approximate the Doppler observation matrix by the direct Doppler measurement for a given set of spherical harmonic coefficients, which facilitate the computation of the least-squares filter.

Utilizing the mathematical development above, the performance of the GM, C_{20}, and C_{22} are presented for a single flyby trajectory. Due to the complexity of matrix inversion and undesirable correlation terms in the information matrix, we process each coefficient one by one. Then, it is shown that GM is best estimated when the inclination and the argument of perigee are both 90° or 270°, irrespective of the right ascension. Comparison of Doppler and OpNav covariance also reports that when the periapsis occurs near the xy-plane, OpNav is a more reliable measurement than Doppler. The C_{20} and C_{22} coefficients are modeled after Bennu and Itokawa, and their covariances are studied for various flyby geometries. It is shown that the C_{20} uncertainties are independent of the rotation rate, as its acceleration is only a function of the latitude, and the rise angle β is parallel to the local transverse axis $\hat{\mathscr{T}}$. The C_{22} uncertainties are more complicated due to its dependence on both latitude and longitude. However, correlation between the rotation rate and β are reported. Generally, the slower the rotation rate corresponds to the higher rise angle.

Finally, the optimal flyby geometries are found by exhaustively searching the three dimensional space

of right ascension, inclination, and argument of perigee for a given target radius/speed. Then, the contour plots of the GM, C_{20}, and C_{22} with respect to the target radius and target flyby speed are presented for the optimal flyby orientation. One notable feature is that the due to the longitudinal dependence of C_{22} acceleration, the contour plot of C_{22} uncertainty has peaks that are functions of the rotation period. In order to verify the applicability of such plots, a different set of target radius/speed are extracted from the contour in order to perform another exhaustive search. The result shows that these uncertainties are consistent with the original contours, validating the consistency between each other.

Acknowledgments

This work has been funded by NASA Near-Earth Object Observations Program as part of the Primitive Body Navigation task and was carried out at the Jet Propulsion Laboratory, California Institute of Technology.

References

[1]Scheeres, D. J., "Satellite Dynamics about Small Bodies: Averaged Solar Radiation," *Journal of Astronautical Sciences*, Vol. 47, 1999, pp. 25 – 46.

[2]Takahashi, Y. and D.J.Scheeres, "Small-Body Postrendezvous Characterization via Slow Hyperbolic Flybys," *Journal of Guidance, Control, and Dynamics*, Vol. 34, No. 6, 2011, pp. 1815 – 1827.

[3]Anderson, J. D., Armstrong, J. W., Campbell, J. K., Estabrook, F. B., Krisher, T. P., and Lau, E. L., "Gravitation and Celestial Mechanics Investigations with Galileo," *Space Science Reviews*, Vol. 60, 1992, pp. 591 – 610.

[4]Rappaport, N. J., Bertotti, B., Giampieri, G., and Anderson, J. D., "Doppler Measurements of the Quadrupole Moments of Titan," *Icarus*, Vol. 126, 1997, pp. 313 – 323.

[5]Anderson, J. D. and Schubert, G., "Rhea's Gravitational Field and Interior Structure Inferred from Archival Data Files of the 2005 Cassini Flyby," *Physics of the Earth and Planetary Interiors*, Vol. 178, 2010, pp. 176 – 182.

[6]Pätzold, M., Wennmacher, A., Häusler, B., Eidel, W., Morley, T., Thomas, N., and Anderson, J. D., "Mass and Density Determinations of 140 Siwa and 4979 Otawara as Expected from the Rosetta Flybys," *Astronomy and Astrophysics*, Vol. 370, 2001, pp. 1122 – 1127.

[7]Pätzold, M., Andert, T. P., Asmar, S. W., Anderson, J. D., Barriot, J.-P., Bird, M. K., Häusler, B., Hahn, M., Tellmann, S., Sierks, H., Lamy, P., and Weiss, B. P., "Asteroid 21 Lutetia: Low Mass, High Density," *Science*, Vol. 334, 2011, pp. 491.

[8]Pätzold, M., Andert, T. P., Häusler, B., Tellmann, S., Anderson, J. D., Asmar, S. W., Barriot, J.-P., and Bird, M. K., "Pre-flyby Estimates of the Precision of the Mass Determination of Asteroid (21) Lutetia from Rosetta Radio Tracking," *Astronomy and Astrophysics*, Vol. 518, 2010.

[9]Veverka, J., Thomas, P., Harch, A., Clark, B., III, J. B., Carcich, B., Joseph, J., Chapman, C., Merline, W., Robinson, M., Malin, M., McFadden, L. A., Murchie, S., III, S. E. H., Farquhar, R., Izenberg, N., and Cheng, A., "Near's Flyby of 253 Mathilde: Images of a C Asteroid," *Science*, Vol. 278, 1997, pp. 2109 – 2114.

[10]Yeomans, D. K., Barriot, J.-P., Dunham, D. W., Farquhar, R. W., Giorgini, J. D., Helfrich, C. E., Konopliv, A. S., McAdams, J. V., Miller, J. K., Jr., W. M. O., Scheeres, D. J., Synnott, S. P., and Williams, B. G., "Estimating the Mass of Asteroid 253 Mathilde from Tracking Data during the NEAR Flyby," *Science*, Vol. 278, 1997, pp. 2106 – 2109.

[11]Anderson, J. D., Jacobson, R. A., and McElrath, T. P., "Shape, Mean Radius, Gravity Field, and Interior Structure of Galileo," *Icarus*, Vol. 153, 2001, pp. 157 – 161.

[12]Anderson, J. D., Schubert, G., Jacobson, R. A., Lau, E. L., Moore, W. B., and Sjogren, W. L., "Europa's Differentiated Internal Structure: Inferences from Four Galileo Encounters," *Science*, Vol. 281, 1998, pp. 2019 – 2022.

[13]Anderson, J. D., "Feasibility of Determining the Mass of an Asteroid from a Spacecraft Flyby," *Physical Studies of Minor Planets: IAU Colloq. 12*, Vol. NASA SP-267, 1971, pp. 577.

[14]Sybert, C. B., Jones, J. B., and Anderson, J. D., "Small Body Mass Determination from a Flyby," *AAS/AIAA Spaceflight Mechanics Meeting, Houston, TX*, , No. 91-166, February 1991, pp. 885 –896.

[15]Anderson, J. D. and Giampieri, G., "Theoretical Description of Spacecraft Flybys by Variation of Parameters," *Icarus*, Vol. 138, 1999, pp. 309 – 318.

[16]Rappaport, N. J., Giampieri, G., and Anderson, J. D., "Perturbations of a Spacecraft Orbit during a Hyperbolic Flyby," *Icarus*, Vol. 150, 2001, pp. 168 – 180.

[17]Takahashi, Y. and Scheeres, D., "Small Body Surface Gravity Fields via Spherical Harmonic Expansions," *Celestial Mechanics and Dynamical Astronomy*, Vol. 119, No. 2, 2014, pp. 169 – 206.

[18]Kaula, W. M., *Theory of Satellite Geodesy*, chap. 1, Blaisdell Publishing Company, Waltham, Massachusetts, 1966.

[19]Takahashi, Y., Busch, M. W., and Scheeres, D. J., "Spin State and Moment of Inertia Characterization of 4179 Toutatis," *The Astronomical Journal*, Vol. 146:95, No. 4, 2013.

[20]Nolan, M., Magri, C., Howell, E., Benner, L. A. M., Giorgini, J. D., Hergenrother, C., Hudson, R., Lauretta, D., Margot, J.-L., Ostro, S., and Scheeres, D., "Shape Model and Surface Properties of the OSIRIS-REx Target Asteroid (101955) Bennu from Radar and Lightcurve Observations," *Icarus*, Vol. 226, February 2013, pp. 629–640.

[21]Scheeres, D. J., Gaskell, R., Abe, S., Barnouin-Jha, O., Hashimoto, T., Kawaguchi, J., Kubota, T., Saito, J., Yoshikawa, M., Hirata, N., Mukai, T., Ishiguro, M., Kominato, T., Shirakawa, K., and Uo, M., "The Actual Dynamical Environment About Itokawa," *AIAA/AAS Astrodynamics Specialist Meeting*, August 2006.